Mechanisms and dynamics of the $NH_2^+ + H^+$ and $NH^+ + H^+ + H$ fragmentation channels upon single-photon double ionization of NH_3

Kirk A Larsen[1,2,*], Thomas N Rescigno[2], Zachary Streeter[2,3], Wael Iskandar[2], Saijoscha Heck[2,4,5], Averell Gatton[2,6], Elio G Champenois[1,2], Travis Severt[7], Richard Strom[6], Bethany Jochim[7], Dylan Reedy[8], Demitri Call[8], Robert Moshammer[4], Reinhard Dörner[5], Allen L Landers[6], Joshua B Williams[8], C William McCurdy[2,3], Robert R Lucchese[2], Itzik Ben-Itzhak[7], Daniel S Slaughter[2] and Thorsten Weber[2,*]

[1] Graduate Group in Applied Science and Technology, University of California, Berkeley, CA 94720, United States of America
[2] Chemical Sciences Division, Lawrence Berkeley National Laboratory, Berkeley, CA 94720, United States of America
[3] Department of Chemistry, University of California, Davis, CA 95616, United States of America
[4] Max-Planck-Institut für Kernphysik, Saupfercheckweg 1, 69117 Heidelberg, Germany
[5] Institut für Kernphysik, J W Goethe Universität, Max-von-Laue-Str. 1, 60438 Frankfurt, Germany
[6] Department of Physics, Auburn University, AL 36849, United States of America
[7] J R Macdonald Laboratory, Physics Department, Kansas State University, Manhattan, KS 66506, United States of America
[8] Department of Physics, University of Nevada Reno, Reno, NV 89557, United States of America

*Corresponding authors E-mail: klarsen@lbl.gov, tnrescigno@lbl.gov and tweber@lbl.gov

Published 19 November 2020

Abstract

We present state-selective measurements on the $NH_2^+ + H^+$ and $NH^+ + H^+ + H$ dissociation channels following single-photon double ionization at 61.5 eV of neutral NH_3, where the two photoelectrons and two cations are measured in coincidence using 3D momentum imaging. Three dication electronic states are identified to contribute to the $NH_2^+ + H^+$ dissociation channel, where the excitation in one of the three states undergoes intersystem crossing prior to dissociation, producing a cold NH_2^+ fragment. In contrast, the other two states directly dissociate, producing a ro-vibrationally excited NH_2^+ fragment with roughly 1 eV of internal energy. The $NH^+ + H^+ + H$ channel is fed by direct dissociation from three intermediate dication states, one of which is shared with the $NH_2^+ + H^+$ channel. We find evidence of autoionization contributing to each of the double ionization channels. The distributions of the relative emission angle between the two photoelectrons, as well as the relative angle between the recoil axis of the molecular breakup and the polarization vector of the ionizing field, are also presented to provide insight on both the photoionization and photodissociation mechanisms for the different dication states.

Keywords: photoionization, photodissociation, COLTRIMS, double ionization, intersystem crossing, non-adiabatic dynamics, autoionization

1. Introduction

Molecular dissociation of polyatomic systems that follows single photon double ionization (PDI) can involve an excitation to a given dication electronic state reaching its own respective adiabatic limit or undergoing non-adiabatic transitions between states preceding the fragmentation [1–3]. Non- adiabatic dynamics, e.g., ultrafast state coupling via conical intersections (CIs) in polyatomic molecules, occur often. CIs are degeneracies between Born–Oppenheimer potential energy surfaces (PESs) that result in non-adiabatic transitions between excited states. They can be facilitated via (a) internal conversion, where two interacting hypersurfaces have the same multiplicity, or (b) intersystem crossing processes, where the multiplicity is different and spin–orbit coupling is required. Both flavors (a) and (b) represent a breakdown of the Born–Oppenheimer approximation [4]. CIs have been observed in numerous instances to significantly shape the molecular fragmentation processes occurring in the molecular dication, influencing the branching ratios, energy dispersion, breakup kinematics, and timescales [1–3]. However, identifying the flavor of the CI, i.e., distinguishing between type (a) and (b), by precisely tracing the electron and nuclear dynamics between the instant of PDI and when the dissociation has set in, is very challenging. This is because polyatomic molecules can break up in many different ways after PDI, and each reaction channel inherently carries different coupled rovibrational degrees of freedom that can be excited. Some of these non-adiabatic fragmentation dynamics leave their fingerprint in the energy or momentum domain of the emitted particles, and they can be determined if the 3D momenta of the photoelectron-pair and the recoiling fragments can be measured in coincidence to produce highly differential observables, which is the aim of this work. In this paper we report on the PDI of NH_3 and reveal the role and flavor of a non-adiabatic transition occurring in a select two-body breakup channel, while identifying the other two- and three-body breakup channels as direct, in a combined effort of experiment and theory.

The electronic states of NH_3^{2+} and its dissociation channels have been studied in detail experimentally following PDI, electron impact double ionization, and double-charge-transfer spectroscopy, as well as theoretically [5–21]. These studies have largely focused on establishing the appearance energies of the various dissociation channels and the relative energies of the dication electronic states. Early experimental studies on the two-body $NH_2^+ + H^+$ dissociation channel in a narrow photon energy range near the PDI threshold revealed that intersystem crossing from the $X\ (3a_1^{-2})\ ^1A_1$ to the $A\ (3a_1^{-1}, 1e^{-1})\ ^3E$ state can facilitate fragmentation [21]. However, non-adiabatic effects have remained unobserved in any of the other fragmentation channels, whether near or well above the double ionization threshold. Additionally, to our knowledge, no study to date has examined the exact nature of the PDI mechanisms in NH_3 in detail, e.g. the level at which autoionization contributes to the PDI, if at all, or if the PDI is primarily based on an electron–electron knock-out process (so called two-step 1 interaction [22]).

In our recent study [23], hereafter referred to as [I], we reported the photoionization mechanisms and photodissociation dynamics of the $H^+ + H^+$ fragmentation channels of NH_3^{2+} following PDI of neutral NH_3 molecules at 61.5 eV. In that study we observed non-adiabatic dynamics that enables both a sequential dissociation mechanism and a charge transfer process. In this report we extend our investigation to the $NH_2^+ + H^+$ and $NH^+ + H^+ + H$ dissociation channels of NH_3^{2+} following PDI of NH_3 molecules at 61.5 eV, approximately 27 eV above the PDI threshold, where both the photoelectron- and cation-pair are measured in coincidence using charged particle 3D momentum imaging.

2 Experiment

Both the $NH_2^+ + H^+$ and $NH^+ + H^+ + H$ fragmentation channels of NH_3^{2+} following PDI of neutral NH_3 molecules at 61.5 eV were investigated using cold target recoil ion momentum spectroscopy [24, 25], where the two photoelectrons and two cations produced by PDI are detected with full 4π solid angle, and their 3D momenta are measured in coincidence on an event-by-event basis. The photoelectron- and cation-pair were guided using static parallel electric and magnetic fields, 11.4 V cm^{-1} and 10.0 G, respectively, to multi-hit capable position- and time-sensitive detectors. The detectors comprised a multi-channel plate (MCP) stack in chevron configuration, backed by a delay-line anode readout, each at opposite ends of the spectrometer. The electron and ion delay-line detectors were a three-layer hex-anode with an 80 mm MCP stack and a two-layer quad-anode with a 120 mm MCP stack, respectively. This system encodes a charged particle's 3D momentum into its hit position on the detector and time-of-flight (TOF) relative to the incoming XUV light pulses. These detectors are subject to multi-hit dead-time effects that are most prominent in the electron pair detection, due to the small variation in the electron's arrival times and hit positions on the detector [26], whereas the dead-time effects play a negligible role for the detection of the cation pair. This dead-time effect can influence the measured relative electron–electron angular distribution, hence it is important to quantify this deficiency, in order to distinguish real features from those which originate from the underperforming detection scheme. The electron-pair resolution is estimated by simulating

the relative motion of the electron pair in the spectrometer fields with various electron sum kinetic energies and in various electron energy sharing conditions. For each pair of electron trajectories, the relative hit position and TOF is computed, which is used to determine the fraction of simulated electron-pair events lost due to an estimated detector response, and thus approximate the fraction of actual losses.

PDI was performed using a linearly polarized tunable monochromatic beam of extreme ultraviolet (XUV) photons produced at beamline 10.0.1.3. at the advanced light source, located at Lawrence Berkeley National Laboratory. The beamline monochromator was configured to provide 61.5 eV photons to the experiment with an energy resolution of less than ±50 meV. The photon energy of 61.5 eV was chosen to be near the maximum of the PDI cross section of NH_3, while at the same time providing electron kinetic energies that can be detected with full solid angle and adequate energy resolution (around 1:10). Moreover, it is beneficial to keep the electron sum energy greater than ~5 eV in order to utilize a large region of the 3D electron pair detection phase space, minimizing losses due to the electron detector dead-time.

A beam of rotationally and vibrationally cold (~80 K) NH_3 molecules (Praxair, anhydrous ammonia >99% purity) was produced by an adiabatic expansion of pressurized gas through a 50 μm nozzle and collimated by a pair of downstream skimmers. The first skimmer had a diameter of 0.3 mm, and the second skimmer had a diameter of 0.5 mm. The first skimmer was placed 8 mm downstream of the nozzle and in the zone of silence of the supersonic expansion. The second skimmer was 10 mm downstream of the first skimming stage. This supersonic gas jet propagated perpendicular to the photon beam, where the two beams crossed at the interaction region (~0.15×0.15×1.0 mm^3) inside the 3D momentum imaging spectrometer, resulting in the PDI of neutral ammonia in its ground state at an average rate of less than 0.01 events per XUV pulse, assuring unambiguous coincidence conditions. The pressure in the target chamber was ~2×10^{-8} Torr with the supersonic beam running and was approximately a factor of 2 lower without the jet. The target gas itself was delivered through a room temperature injection line using Swagelok connections. Background water in the target chamber was the largest contaminating species and was minimized using a cold trap filled with liquid nitrogen.

The TOF and hit position of charge particles produced by the PDI were recorded in list mode on an event-by-event basis, enabling relevant events to be captured and examined in a detailed off-line analysis, using the LMF2Root software package [27] described in reference [28]. After cleaning, calibrating, and sorting the data set, for each PDI event the photoelectron kinetic energy was determined from the 3D photoelectron momentum, while the kinetic energy release (KER) of the fragmentation was determined from the 3D momenta of the two cations. We inferred the momentum of the neutral H fragment in the three-body dissociation channel from momentum conservation.

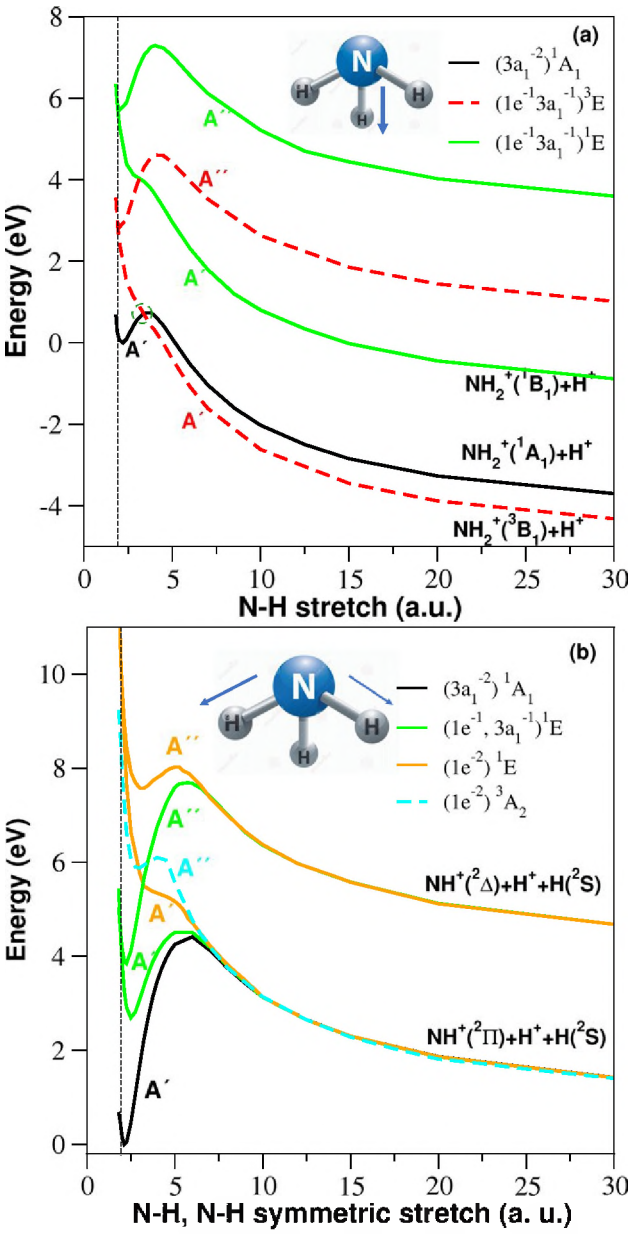

Figure 1. PES cuts of the experimentally identified states of the NH_3 dication generated from MRCI calculations as described in the text. In panel (a) one hydrogen is stretched while the other two hydrogens remain fixed, with all internal angles frozen at the geometry of neutral ammonia. In panel (b) two hydrogens are symmetrically stretched while the third hydrogen remains fixed, with all internal angles frozen at the geometry of neutral ammonia. The dissociation limits are given in table 1. The zero of energy is set to the ground-state ($^1A_1$) of the ammonia dication at the geometry of the neutral ammonia molecule, which lies 34.8 eV below the dication ground state [8]. On this energy scale, the 61.5 eV photon energy falls at 26.74. The green dashed circle in panel (a) indicates the region where intersystem crossing may occur. The broken vertical lines indicate the equilibrium geometry of neutral NH_3.

3. Theory

The electron configuration of neutral NH_3 in its ground-state is $(1a_1)^2(2a_1)^2(1e)^4(3a_1)^2$. Nine low-lying singlet and triplet states of the ammonia dication can be formed by distributing six electrons over the outer $1e$ and/or $3a_1$ orbitals, all of

Table 1. Ammonia dication vertical energies at neutral NH_3 geometry and asymptotic two- and three-body dissociation limits extrapolated from *ab initio* calculations at N–H distances of 30.0 Bohr (see text). The zero of energy is set to the ground-state ($^1A_1$) of the ammonia dication at the geometry of the neutral ammonia molecule.

State	Vertical energy (eV)	Asymptote	Adiabatic limit energy (eV)
		Two-body channels	
$(3a_1^{-2})\ ^1A_1$ (black)	0.44	$NH_2^+(^1A_1) + H^+$	−4.61
$(1e^{-1}, 3a_1^{-1})^3E$(red)	2.97	$NH_2^+\ (^3B_1) + H^+$	−5.23
$(1e^{-2})\ ^1E$ (gold)	5.74	$NH_2^+\ (^1B_1) + H^+$	−3.09
		Three-body channels	
$(3a_1^{-2})\ ^1A_1$ (black)	0.44	$NH^+\ (^2\Pi) + H^+ + H$	0.52
$(1e^{-1}, 3a_1^{-1})\ ^1E[A^{\mathrm{I}}]$ (green)	5.74	$NH^+\ (^2\Pi) + H^+ + H$	0.52
$(1e^{-1}, 3a_1^{-1})\ ^1E[A^{\mathrm{II}}]$ (green)	5.74	$NH^+\ (^2\Delta) + H^+ + H$	3.78
$(1e^{-1}, 3a_1^{-1})\ ^3A_2$ (cyan)	8.64	$NH^+\ (^2\Pi) + H^+ + H$	0.52
$(1e^{-2})\ ^1E[A']$ (gold)	10.39	$NH^+\ (^2\Pi) + H^+ + H$	0.52
$(1e^{-2})\ ^1E[A'']$ (gold)	10.39	$NH^+\ (^2\Delta) + H^+ + H$	3.78

which are accessible by single photon absorption at an energy of 61.5 eV. In order to determine which of these states correlate with the two-body $NH_2^+ + H^+$ dissociation channel and three-body $NH^+ + H^+ + H$ fragmentation channel, we carried out a series of electronic structure calculations, analogous to those described in [I]. As in our recent work, the molecular orbitals at each geometry considered were generated from state-averaged, complete active space (CAS) multi-configuration self-consistent field calculations on the two lowest triplet (^3E) states of the dication, keeping one orbital (N 1*s*) frozen and including seven orbitals in the CAS space. These were followed by multi-reference configuration-interaction (MRCI) calculations, including all single and double excitations from the CAS reference space, to generate cuts through the calculated PESs. As in [I], all bond angles were frozen at the equilibrium geometry of neutral ammonia (107°), as was one hydrogen bond length (1.9138 Bohr), while either one or two hydrogen bonds were stretched. The results of the calculations are shown in figures 1(a) and (b), respectively. The electron configuration and state labels of each dication PES are given in the legend. The vertical energies at the neutral NH_3 geometry and the energies at the asymptotic limits (extrapolated from 30 Bohr to infinity under the assumption of a purely repulsive Coulomb interaction between the positively charged fragments) are given in table 1.

Our calculations reveal that there are five relevant dication electronic states accessible in the Franck–Condon (FC) region. Three of these states are singlets, $(3a_1^{-2})\ ^1A_1$, $(3a_1^{-1}, 1e^{-1})\ ^1E$, and $(1e^{-2})\ ^1E$, shown as solid curves (black, green, and gold), while two are triplets, $(3a_1^{-1}, 1e^{-1})\ ^3E$, and $(1e^{-2})\ ^3A_2$ shown as dashed curves (red and cyan).

In the case of stretching a single proton (asymmetric stretch), figure 1(a) shows that the three NH_3^{2+} states $(3a^{-2})\ ^1A_1$, $(3a_1^{-1}, 1e^{-1})\ ^3E$, and $(3a_1^{-1}, 1e^{-1})\ ^1E$ correlate with the $^1A_1$, $^3B_1$, and $^1B_1$ states of NH_2^+, respectively. The $(3a^{-2})\ ^1A_1$ state is evidently predissociated by the A' component of the ^3E state, which can lead to a non-adiabatic transition between these states via intersystem crossing.

In the case of symmetric stretch of two hydrogen bonds, it can be seen in figure 1(b) that the $^1A'$ components of the $(3a_1^{-1}, 1e^{-1})\ ^1E$, $(1e^{-2})\ ^1E$ states, as well as the $^3A''$ $[(1e^{-2})\ ^3A_2]$ state, all dissociate to the three-body channel $NH^+\ (^2\Pi) + H^+ + H$. The two A'' symmetry components of the $(3a_1^{-1}, 1e^{-1})\ ^1E$ and $(1e^{-2})\ ^1E$ dication states dissociate to $NH^+\ (^2\Delta) + H^+ + H$. Previous measurements have also indicated that the $(1e^{-2})\ ^1E$ dication state dissociates to the $NH^+ + H^+ + H$ channel [6].

To get theoretical estimates of the expected spread of the observed photoelectron energies for the various dication states, we use a variant of the so-called reflection approximation [29]. The range of detectable KERs is determined by the FC envelope of the initial (neutral) vibrational state reflected onto the final dication PESs. For the initial vibrational wavefunction we use a harmonic oscillator function χ_0, obtained from a fit of the ground state energy of ammonia as a function of the symmetric stretch. If we assume that the PDI cross section varies little over the FC region (which is a good approximation, since there are no resonances or near-threshold effects at the chosen photon energy) and that the final continuum vibrational wavefunctions can be approximated by delta functions about the classical turning points on the dication PESs [30], then the envelope of the expected photoelectron energies is given by the values of the vertical PDI energies as a function of the symmetric-stretch coordinate, weighted by the square of the symmetric-stretch vibrational wavefunction. We find that χ_0^2 reaches half its maximum value at a symmetric-stretch displacement of approximately 0.11 Bohr from equilibrium, and we have used these values to calculate the FWHM of the photoelectron distributions below.

4. Results

The $NH^+ + H^+$ two-body and $NH^+ + H^+ + H$ three-body dissociation channels of NH_3^{2+}, following PDI of NH_3 at 61.5 eV, ~27 eV above the PDI threshold, are identified and isolated by selecting the two charged fragments in the photoion–photoion coincidence (PIPICO) TOF spectrum and then in momentum space. Moreover, we also enforce that two electrons are measured in coincidence with the two ionic

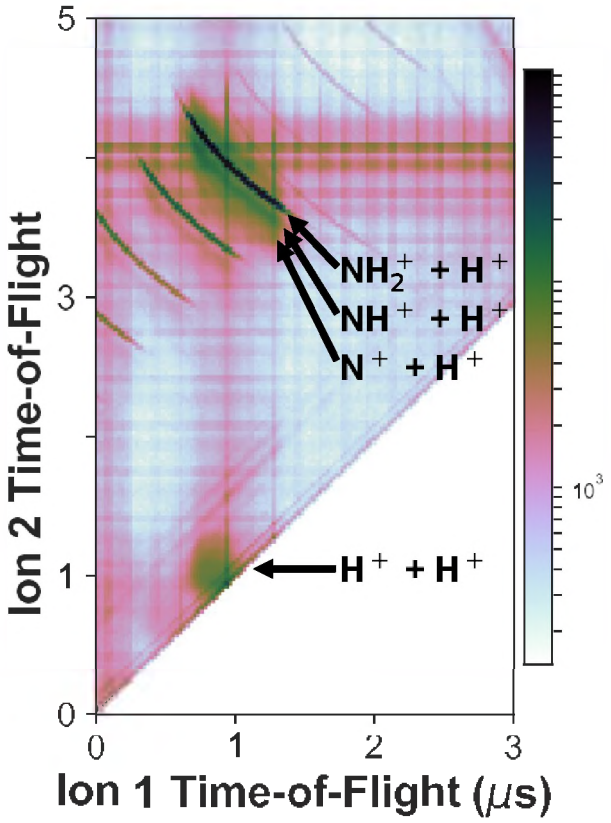

Figure 2. The photoion–photoion TOF coincidence map (PIPICO spectrum), shown on a logarithmic scale. The observed PIPICOs from the respective breakup channels following PDI of NH_3 at 61.5 eV are indicated by the black arrows and text. Two of these channels ($H^+ + H^+$ and $N^+ + H^+$) are the topic of paper [I].

fragments. We show the PIPICO spectrum in figure 2, where the PIPICO yield is shown on a logarithmic scale. Here we observe four PIPICO features following PDI of NH_3 molecules, two of which are addressed in this report, $NH_2^+ + H^+$ and $NH^+ + H^+$, while the other two coincidence features, $H^+ + H^+$ and $N^+ + H^+$, are the topic of manuscript [I]. The $N^+ + H^+$ channel is very faint and diffuse, which renders it difficult to visually identify in the PIPICO spectrum alone, however it emerges upon further analysis (examined in [I]). The vertical and horizontal features, as well as the periodically repeating features, are the result of false coincidences, which are removed later in our analysis. We first begin with a discussion of the $NH_2^+ + H^+$ two-body fragmentation channel before turning to the $NH^+ + H^+ + H$ three-body channel. By inspecting the yield of the two features in the PIPICO corresponding with $NH_2^+ + H^+$ and $NH^+ + H^+$ coincidences, we find the approximate branching ratio between the $NH_2^+ + H^+$ two-body and the $NH^+ + H^+ + H$ three-body dissociation channels to be 86:14.

4.1. *Two-body breakup channel:* $NH_2^+ + H^+$

We plot the PDI yield of the $NH_2^+ + H^+$ fragmentation channel of NH_3^{2+} as a function of the kinetic energy of the first and second detected electrons, to produce an electron–electron energy correlation map, as shown in figure 3. Since the two electrons

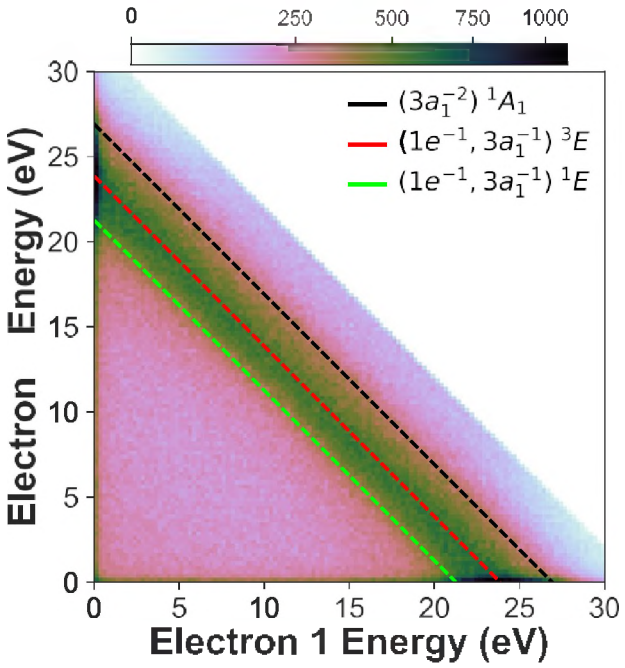

Figure 3. The $NH_2^+ + H^+$ yield as a function of the kinetic energy of the first and second photoelectron after PDI of NH_3 at 61.5 eV. The three features indicating the active dication states are color-coded (black, red, and green) and shown as diagonal lines to guide the eye. Electrons with energy sums beyond 35 eV were not detected with full 4π solid angle and are hence omitted.

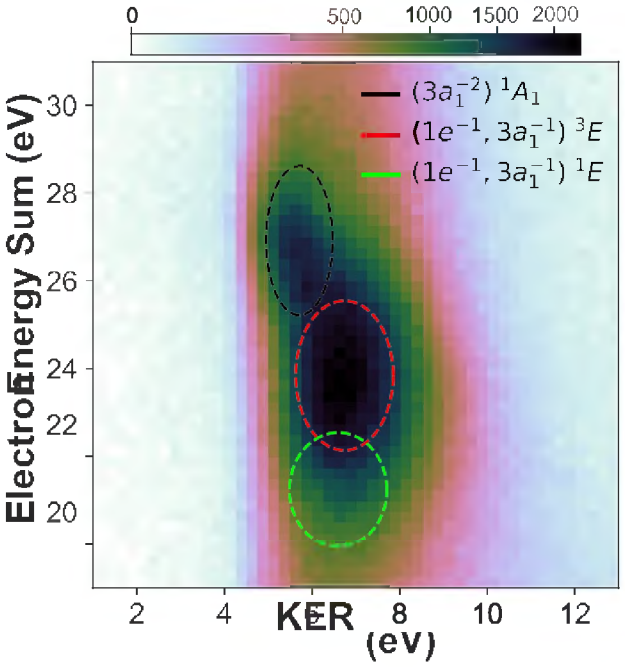

Figure 4. The $NH_2^+ + H^+$ yield as a function of the KER and the kinetic energy sum of the photoelectron pair after PDI of NH_3 at 61.5 eV. The three features indicating the active dication states are color-coded (black, red, and green) and shown as ellipses to guide the eye (they only approximately represent the software gates).

are indistinguishable particles, the labeling (as 1 and 2) is arbitrary, and the figure has been symmetrized across the diagonal

Table 2. The measured and calculated photoelectron energy sum and KER for each of the three identified features from $NH_2^+ + H^+$ fragmentation following PDI of NH_3 at 61.5 eV, as well as the estimated branching ratios and β_2 anisotropy parameter (see text). The energy widths (FWHM) are in parentheses.

State	Photoelectron	Energy sum (eV)	KER (eV)		Branching fraction	β_2
	Experiment	Theory[a]	Experiment	Theory[a,b]		
$(3a_1^{-2})\ ^1A_1$ (black)	26.9 (1.5)	26.5 (1.5)	5.7 (1.0)	5.5 (1.5)	13% ± 3%	−0.30 ± 0.01
$(3a_1^{-1}, 1e^{-1})\ ^3E$ (red)	23.9 (2.0)	23.5 (2.0)	6.7 (1.3)	8.2 (2.0)	44% ± 3%	−0.12 ± 0.01
$(3a_1^{-1}, 1e^{-1})\ ^1E$ (green)	21.4 (1.7)	21.0 (2.4)	6.7 (1.2)	7.5 (2.4)	43% ± 3%	−0.18 ± 0.01

[a] Theoretical FWHM values estimated from the square of the symmetric stretch vibrational wavefunction of NH_3 projected onto the respective dication state (see text).

[b] Theoretical KER values are calculated assuming ro-vibrational ground state fragments, i.e., assuming maximum KER with no energy channeled into internal excitations.

(the line $E_1 = E_2$) to account for this. With the guidance of the calculated PES cuts, we identify three features corresponding with three different NH_3^{2+} electronic states that feed into the $NH_2^+ + H^+$ two-body fragmentation channel. Although difficult to visually identify here, these three features are better separated in different spectra that are shown below in figure 4. Each of these three features correspond to two photoelectrons with energy sums centered around 26.9 eV, 23.9 eV, and 21.4 eV, with a full width at half maximum (FWHM) of roughly 1.5 eV, 2.0 eV, and 1.7 eV, respectively. These features, indicated as diagonal lines (with the form $E_2 = E_1 + E_{sum}$, where E_{sum} is the photoelectron energy sum corresponding to that feature), have been color-coded as black, red, and green to guide the eye. In the offline analysis we choose each of these three features by selecting carefully around the center of each feature in figure 4. Enforcing conditions in a multitude of observables and dimensions (particle energy and momenta) in this fashion enables us to separate these three features for subsequent in-depth analysis.

The FWHM of the electron energy sum of each dication state roughly corresponds with the magnitude of the gradient of the PES in the FC region (convoluted with the energy resolution of the electron detector). The characteristics of the three features suggest that the three dication states are accessed via direct PDI, as indicated by the uniformity of the negatively sloped diagonal features in figure 3, and also appear to be populated through autoionization, the signature being the two sharp features located at the end of the diagonals, where one of the electrons possesses nearly zero kinetic energy. The branching ratio between these three measured channels that correspond with the three dication states shown in table 2 is estimated from the relative yield of these three features. The branching ratios and the method used to estimate them are discussed below.

Next, we plot the yield of the $NH_2^+ + H^+$ dissociation channel as a function of the KER and the kinetic energy sum of the photoelectron pair, in order to generate an electron–ion energy correlation map. Three features corresponding with the three color-coded diagonals in figure 3 are present in the electron–nuclei energy correlation map, shown in figure 4. These three features are marked by ellipses in their respective color-codes to guide the eye (note: these ellipses do not reflect the actual momentum gates of the analysis). The feature circled by the green ellipse is comparatively faint and can be mistaken as a part of the feature circled by the red ellipse, however it is identified as a state with the assistance of the calculated PES cuts. Here we see that each dication state possesses a different distribution of KER centered around 5.7 eV, 6.7 eV, and 6.7 eV, each with a FWHM of roughly 1.0 eV, 1.3 eV, and 1.2 eV, respectively. The FWHM of the KER of each dication state carries similar information as the electron sum energy FWHM, indicating the steepness of the PESs in the FC region (convoluted with the energy resolution of the ion spectrometer).

We present the $NH_2^+ + H^+$ yield as a function of the photoelectron energy sum in figure 5, where each active dication state we identified in figure 4 has been indicated in figure 5 by a distribution in its corresponding color. In the total yield we observe an asymmetric monomodal distribution, exhibiting a rapid rise in yield on the low energy side of the peak and a slower decay in yield on the high energy side of the peak. The wings on the distribution originate from false coincidences and background events that are challenging to eliminate in the analysis, resulting in a near-uniform background (clearly visible in figure 3) underlying the spectrum that causes exaggerated wings.

We show the $NH_2^+ + H^+$ yield as a function of KER in figure 6, where each dication state we identified in figure 4 has been indicated by a distribution in its corresponding color. In the total yield we observe another broad asymmetric monomodal KER distribution with a rapid increase in yield on the low energy side of the peak and a slower decay in yield towards high energy. Both the experimental and theoretically calculated photoelectron energy sums and KERs are shown in table 2, which show good agreement.

These three corresponding dication states were identified using MRCI calculations, as discussed in section 3, and are consistently color-coded throughout the paper. The $(3a_1^{-2})\ ^1A_1$ state is shown in black, the $(3a_1^{-1}, 1e^{-1})\ ^3E$ state in red, and the $(3a_1^{-1}, 1e^{-1})\ ^1E$ state in green. Our ion yield measurements suggest that the branching ratios for these three dication states, shown in table 2, are approximately 13%±3% for the $(3a_1^{-2})\ ^1A_1$ state, 44%±3% for the $(3a_1^{-1}, 1e^{-1})\ ^3E$ state, and 43%±3% for the $(3a_1^{-1}, 1e^{-1})\ ^1E$ state. These branching ratios and errors (plus/minus one standard deviation) are estimated by simultaneously fitting each feature in figure 4 with separate 2D Gaussian distributions (although the distributions may not be explicitly Gaussian, this is nonetheless a good approximation). The fitting procedure

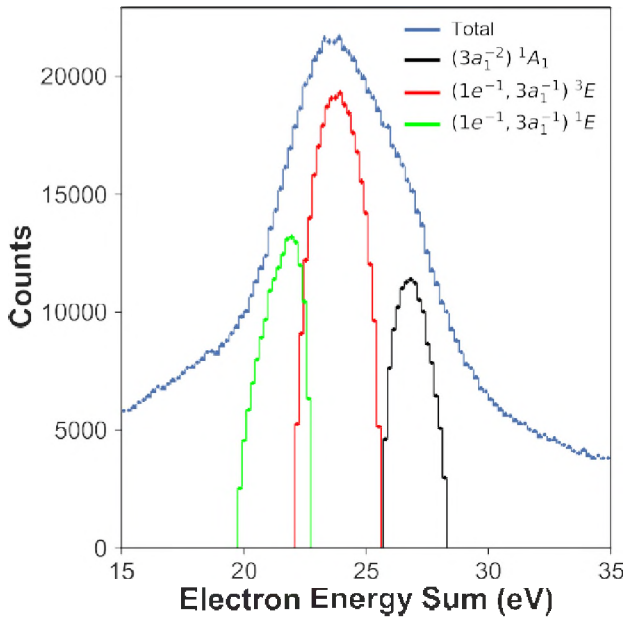

Figure 5. The $NH_2^+ + H^+$ yield as a function of the kinetic energy sum of the photoelectron pair after PDI of NH_3 at 61.5 eV (shown in blue). The distributions for the three contributing dication states are shown in their respective color-codes (shown in black, red, and green, and multiplied by a factor of 1.6 for improved visibility). Contributions from individual dication states are extracted with gates as indicated in figure 4, and hence their sum does not reflect the total (blue) yield (see text). The statistical error bars are on the order of the line width.

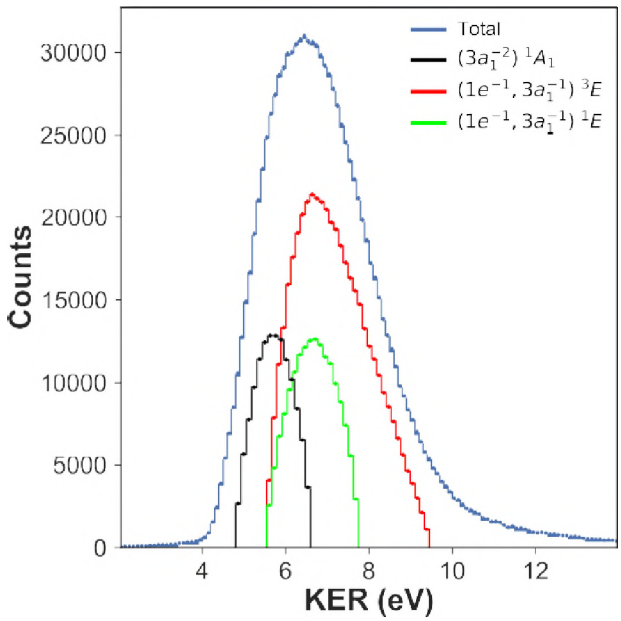

Figure 6. The $NH_2^+ + H^+$ yield as a function of the KER after PDI of NH_3 at 61.5 eV (shown in blue). The distributions for the three contributing dication states are shown in their respective color-codes (shown in black, red, and green, and multiplied by a factor of 1.6 for improved visibility). Contributions from the individual dication states are extracted with gates as indicated in figure 4, and hence their sum does not reflect the total (blue) yield (see text). The statistical error bars are on the order of the line width.

varied the widths along each dimension independently, while also including a varying constant background offset. Following this fitting procedure, we integrate the fit for each dication state to estimate its contribution to the total $NH_2^+ + H^+$ yield. The main contribution to the uncertainty of the branching ratio is rooted in the aforementioned electron pair dead-time, which influences the detection yield of the electron–ion coincidences for each dication state as a function of the electron sum energy. Applying the simulation mentioned above, we estimate the total possible loss in PDI yield for electron sum energies of 26.9 eV [$(3a_1^{-2})\ ^1A_1$], 23.9 eV [$(3a_1^{-1}, 1e^{-1})\ ^3E$], and 21.4 eV [$(3a_1^{-1}, 1e^{-1})\ ^1E$] to be 4.5%, 5.2%, and 5.9%, respectively. This translates to an error of up to 3% in the branching ratio. Errors due to deviations from the assumed Gaussian shape of each feature in the fitting process and the quality of the fit are estimated to be small (both $<1\%$).

From the PES cuts shown in figure 1(a) and the energetics presented in figure 4 and table 2, we conclude that the $(3a_1^{-2})\ ^1A_1$ state dissociates to the $NH_2^+\ (^3B_1) + H^+$ limit, the $(3a_1^{-1}, 1e^{-1})\ ^3E$ state directly dissociates to this very same limit, and the $(3a_1^{-1}, 1e^{-1})\ ^1E$ state directly dissociates to the $NH_2^+\ (^1B_1) + H^+$ limit. Here the $(3a_1^{-2})\ ^1A_1$ dication state must undergo an intersystem crossing preceding the dissociation, as the measured KER indicates that it does not reach its adiabatic limit (which would only produce 5.05 eV of KER). In figure 1(a) it can be seen that the $(3a_1^{-2})\ ^1A_1$ dication state is bound in the FC region and can predissociate by the A' symmetry curve of the $(3a_1^{-1}, 1e^{-1})\ ^3E$ dication state. This enables a non-adiabatic population transfer mechanism that has been observed previously in near-threshold measurements [5, 6]. In reference [5] it was suggested that for excitation energies well above the PDI threshold of NH_3, direct dissocation would dominate over the predissociation, which is enabled by spin–orbit coupling. Our measurement, performed ~27 eV above the double ionization threshold, is at odds with this proposition, as we observe the predissociation via inter-system crossing dominating over direct dissociation. Further, based on the measured KER, we conclude that this coupling mechanism outcompetes the dissociation from the population tunneling through the barrier of the $(3a_1^{-2})\ ^1A_1$ dication state along the asymmetric stretch coordinate, since dissociation via tunneling would result in a lower KER than what is measured. Comparing the measured and calculated KERs for the $(3a_1^{-2})\ ^1A_1$ state (see table 2) indicates that the resulting NH_2^+ fragment is formed in a relatively cold ro-vibrational state. In contrast to the $(3a_1^{-2})\ ^1A_1$ state, the $(3a_1^{-1}, 1e^{-1})\ ^3E$ state directly dissociates on the A'curve, producing an NH_2^+ fragment with approximately 1.5 eV of ro-vibrational energy, which we infer by comparing the measured KER to the theoretical KER calculated for NH_2^+ ground state fragments. However, the $(3a_1^{-1}, 1e^{-1})\ ^3E$ state also exhibits contributions from ro-vibrationally cold NH^+ fragments that reside in the long tail of the KER toward high energy values at constant electron sum energy. Here, a population transfer from the dissociative $(3a_1^{-1}, 1e^{-1})\ ^3E$ dication state to the $(3a_1^{-2})\ ^1A_1$ state is unlikely, as this would involve a non-adiabatic transition between states of different spin symmetry, and the wavepacket would only encounter the coupling region once as it dissociates. Similarly,

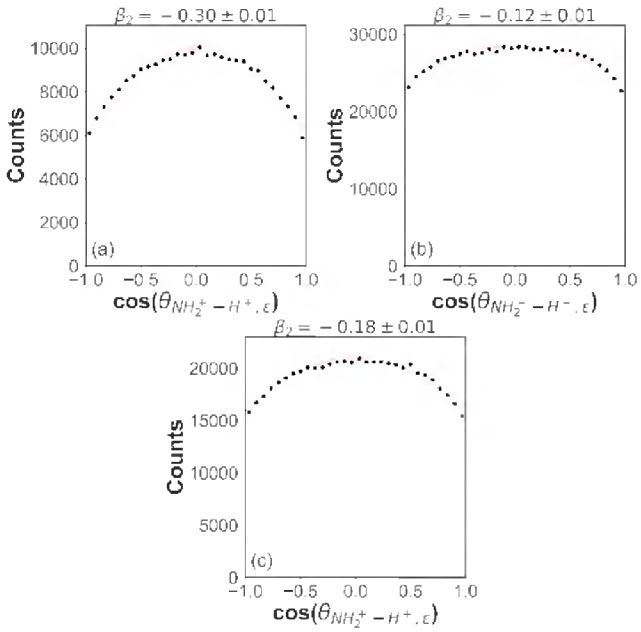

Figure 7. The yield of $NH_2^+ + H^+$ dissociation after PDI of NH_3 at 61.5 eV as a function of the cosine of the measured relative angle between the NH_2–H recoil axis and XUV polarization vector ε for the (a) $(3a_1^{-2})\ ^1A_1$, (b) $(3a_1^{-1}, 1e^{-1})\ ^3E$, and (c) $(3a_1^{-1}, 1e^{-1})\ ^1E$ dication states. The fits, representing the parametrizations in terms of the anisotropy [see equation (1)], are shown in red, where the retrieved β_2 value is shown above each plot.

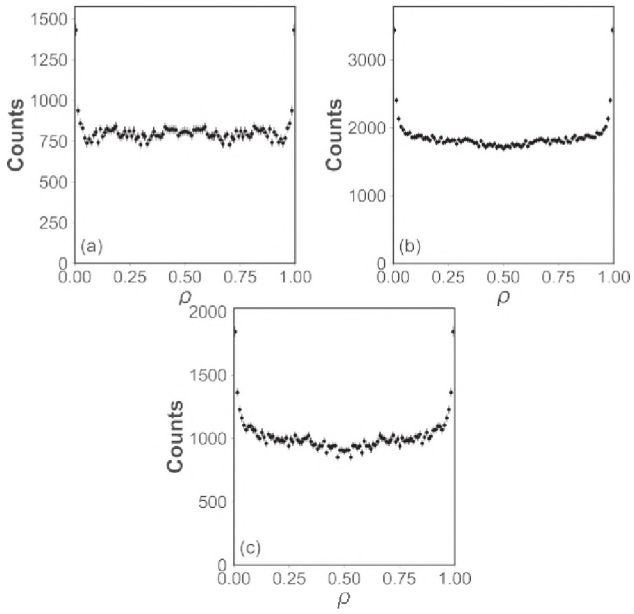

Figure 8. The yield of the $NH^+ + H^+$ two-body breakup after PDI of NH_3 at 61.5 eV as a function of the electron energy sharing ρ [see equation (2)] for the (a) $(3a_1^{-2})\ ^1A_1$, (b) $(3a_1^{-1}, 1e^{-1})\ ^3E$, and (c) $(3a_1^{-1}, 1e^{-1})\ ^1E$ dication states.

the $(3a_1^{-1}, 1e^{-1})\ ^1E$ dication state also directly dissociates on its A' curve, producing an NH_2^+ fragment with approximately 0.8 eV of ro-vibrational energy. We point out that the direct dissociation, producing a ro-vibrationally excited fragment, is consistent with the results in [I].

In order to assess if there are preferred molecular orientations at which PDI of NH_3 occurs for each of the three NH_3^{2+} dication states, we plot in figures 7(a)–(c) the yield of the $NH_2^+ + H^+$ two-body fragmentation as a function of the cosine of the relative angle between the recoil axis of the molecular breakup (NH_2^+–H^+) and the XUV polarization ε. For the features corresponding with the $(3a_1^{-2})\ ^1A_1$, and $(3a_1, 1e^{-1})\ ^3E$, and $(3a_1^{-1}, 1e^{-1})\ ^1E$ dication states, we observe an enhancement in PDI for molecular orientations where the recoil axis is aligned at 90° angle with respect to the polarization vector. Here, this enhancement in PDI yield is strongest in the $(3a_1^{-2})\ ^1A_1$ state, weaker in the $(3a_1^{-1}, 1e^{-1})\ ^1E$ state, whereas the distribution of the $(3a_1^{-1}, 1e^{-1})\ ^3$E dication state is the most isotropic of the three (its β_2 value is the closest to zero). This perpendicular orientation of the recoil axis with respect to the polarization vector roughly coincides with the C_{3v} symmetry axis of the NH_3 molecule. In all dication states the PDI involves the $3a_1$ orbital, i.e., the lone pair, which is aligned along the molecular C_{3v} axis. This could explain the enhancement at geometries where the polarization vector of the ionizing field is directed along this orbital and the stronger effect in the $(3a_1^{-2})\ ^1A_1$ state, where both holes are created in the 3a1 orbital, as opposed to the $(3a_1^{-1}, 1e^{-1})\ ^3E$ and $(3a_1^{-1}, 1e^{-1})\ ^1E$ states, where a hole is created in each of the $3a_1$ and $1e$ orbitals.

These photofragment angular distributions have been fitted (solid red line) using the familiar parameterization:

$$\frac{d\sigma}{d\Omega} = \frac{\sigma_0}{4\pi}[1 + \beta_2 P_2(\cos\theta)], \qquad (1)$$

which describes the fragment angular distribution from the dissociation of a rigid rotor, where σ_0 is the total cross section, β_2 is the anisotropy parameter, P_2 is the second order Legendre polynomial, and θ is the angle between the recoil axis of the molecular two-body breakup and the polarization vector of the ionizing field [31, 32]. The retrieved β_2 parameter is shown above each plot, while the data is fitted using the projection method discussed in [33], where the error of β_2 is determined via statistical bootstrapping [34]. We find β_2 values of -0.30±0.01, -0.12±0.01, and -0.18±0.01 for the $(3a_1^{-2})\ ^1A_1$, $(3a_1^{-1}, 1e^{-1})\ ^3E$, and $(3a_1^{-1}, 1e^{-1})\ ^1E$ dication states, respectively. These values are also listed in table 2.

Next, we display the yield of the $NH_2^+ + H^+$ two-body channel as a function of the energy sharing ρ between the two photoelectrons for the three features that correspond with the three NH_2^+ states. We define the electron energy sharing as:

$$\rho = E_{e1} / [E_{e1} + E_{e2}] \qquad (2)$$

where E_{e1} and E_{e2} are the kinetic energies of electron 1 and 2, respectively. Values of ρ near 0.5 indicate equal energy sharing between the two photoelectrons, while values near 0 or 1 indicate unequal energy sharing between the two photoelectrons. The results are shown in figures 8(a)–(c).

We attribute the sharp features near 0 and 1, observed in figures 8(a)–(c), to the PDI of NH_3 via autoionization, corresponding with a fast photoelectron and slow electron emerging from the autoionization. The fraction of PDI via

autoionization relative to direct PDI is approximately 1.9%±1.0% in the $(3a_1^{-2})\ ^1A_1$ state, 4.4% ±0.7% in the $(3a_1^{-1}, 1e^{-1})\ ^3E$ state, and 6.2%±0.9% in the $(3a_1^{-1}, 1e^{-1})\ ^1E$ state. This is estimated by extrapolating the average number of counts in the equal energy sharing condition across all ρ and then subtracting this value from the bins where ρ is near 0 or 1 (the unequal energy sharing condition). Computing this residue gives an estimate on how many counts are associated with autoionization relative to the direct PDI of NH_3. The error in the autoionization fraction is determined from the error in the average number of counts in the equal energy sharing condition (which is extracted from Poisson statistics).

Finally, we plot in figures 9–11 the yield of the $NH_2^+ + H^+$ dissociation channel as a function of the cosine of the relative emission angle between the two photoelectrons, (a) integrated over all energy sharing conditions and (b) for equal energy sharing condition for the three NH_3^{2+} states. In these figures, there are no conditions enforced on either the molecular orientation or the emission angle of the first detected photoelectron relative to the polarization vector of the XUV beam. In the equal energy sharing case the relative angle is plotted for $0.475 < \rho < 0.525$. We point out that our measurement suffers from some multi-hit detector dead-time effects, which influence the measured yield of photoelectrons emitted in the same direction with similar kinetic energies. In the equal energy sharing condition and for the emission into the same hemisphere $\theta_{e_1,e2} \leq 90°$, this corresponds, in worst case, to a loss of ~15% of the events for the $(3a_1^{-2})\ ^1A_1$ state, ~16% for the $(3a_1^{-1}, 1e^{-1})\ ^3E$ state, and ~18% for the $(3a_1^{-1}, 1e^{-1})\ ^1E$ state. This worst-case scenario is simulated for an isotropic relative electron–electron emission, which very well represents autoionization processes that are sequential in nature and are subject to unequal energy sharing between the electrons. The equal energy sharing case on the other hand is dominated by knock-out processes with very few electron pairs emitted into the same hemisphere. The actual losses are hence believed to be smaller by at least a factor of 2, i.e., closer to the simulated losses for unequal electron energy sharing. We refrain from showing the measured photoelectron angular distribution in the unequal energy sharing case, which captures the autoionization feature, as there is a significant contribution due to direct PDI that pollutes the autoionization signal considerably and prevents a clear analysis of the relative angular distribution for this indirect ionization process.

The relative angles between the two electrons, integrated over all energy sharing cases, show a preferred emission of the two electrons into opposite hemispheres. The distribution for the $(3a_1^{-2})\ ^1A_1$ dication state [figure 9(a)] peaks at 145° with a notable dip at 180° corresponding to a back-to-back emission. The $(3a_1^{-1}, 1e^{-1})\ ^3E$ state [figure 10(a)] peaks at 125° and has a similar dip at 180°. The $(3a_1^{-1}, 1e^{-1})\ ^1E$ state [figure 11(a)] peaks at 120°, with a slight increase at 180° compared to the two other dication states.

The photoelectron dynamics in the equal energy sharing condition ($\rho = 0.5 \pm 0.025$) reveals similar anisotropic angular distributions depicted in figures 9(b)–11(b), which possess minima near 0° relative emission angle in all three states and

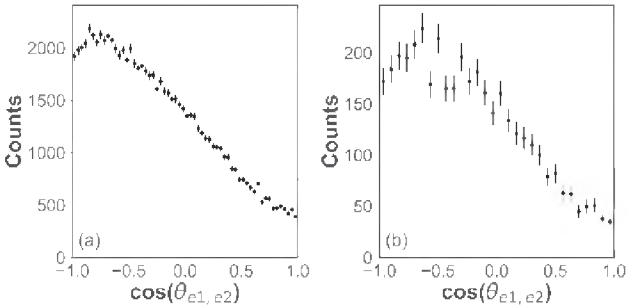

Figure 9. The yield of the $NH_2^+ + H^+$ two-body breakup, after PDI of NH_3 at 61.5 eV, as a function of the cosine of the relative emission angle between the two photoelectrons for the $(3a_1^{-2})\ ^1A_1$ dication state (a) integrated over all possible electron energy sharing and (b) for equal energy sharing ($\rho = 0.5 \pm 0.025$).

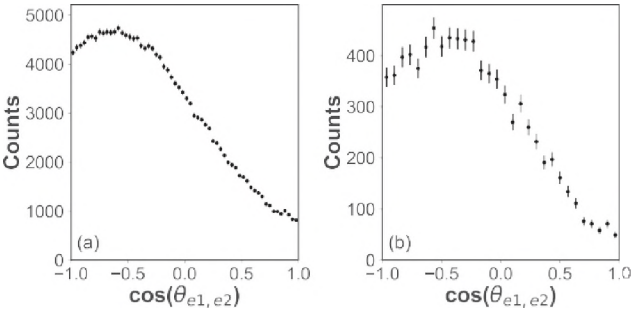

Figure 10. The yield of the $NH_2^+ + H^+$ two-body breakup, after PDI of NH_3 at 61.5 eV, as a function of the cosine of the relative emission angle between the two photoelectrons for the $(3a_1^{-1}, 1e^{-1})\ ^3E$ dication state (a) integrated over all possible electron energy sharing and (b) for equal energy sharing ($\rho = 0.5 \pm 0.025$).

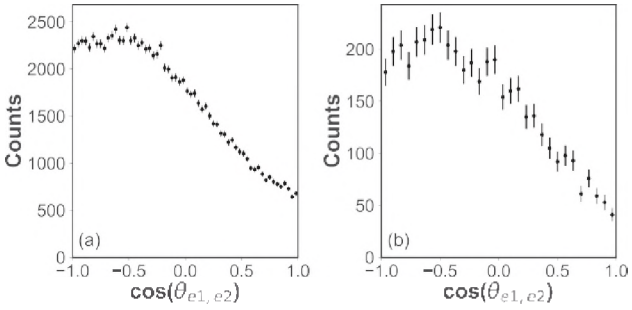

Figure 11. The yield of the $NH_2^+ + H^+$ two-body breakup, after PDI of NH_3 at 61.5 eV, as a function of the cosine of the relative emission angle between the two photoelectrons for the $(3a_1^{-1}, 1e^{-1})\ ^1E$ dication state (a) integrated over all possible electron energy sharing and (b) for equal energy sharing ($\rho = 0.5 \pm 0.025$).

peak at relative angles near 130° in the $(3a_1^{-2})\ ^1A_1$ state, 125° in the $(3a_1^{-1}, 1e^{-1})\ ^3E$ state, and 120° in the $(3a_1^{-1}, 1e^{-1})\ ^1E$ state. All three distributions show a dip at 180°. This relative electron emission pattern is reminiscent of a knock-out double ionization process as found in other valence PDI investigations of atomic and molecular targets [35–38]. In all three cases the likelihood for emission in the same direction is roughly a factor of 10 less likely than emission at the peak angle.

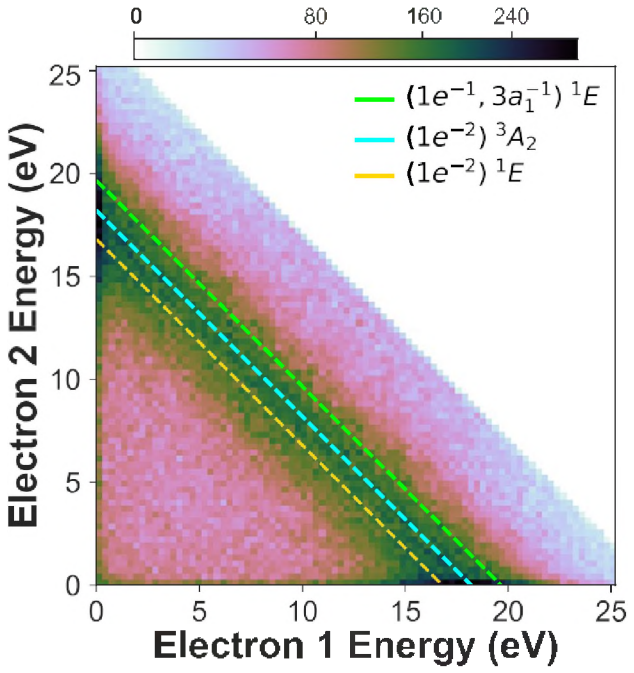

Figure 12. The $NH^+ + H^+ + H$ three-body yield, after PDI of NH_3 at 61.5 eV, as a function of the kinetic energy of the first and second photoelectron. The three contributing dication states are color-coded (green, cyan, and gold) and shown as diagonal lines to guide the eye. Electron sum energies beyond 27 eV are omitted for visual clarity.

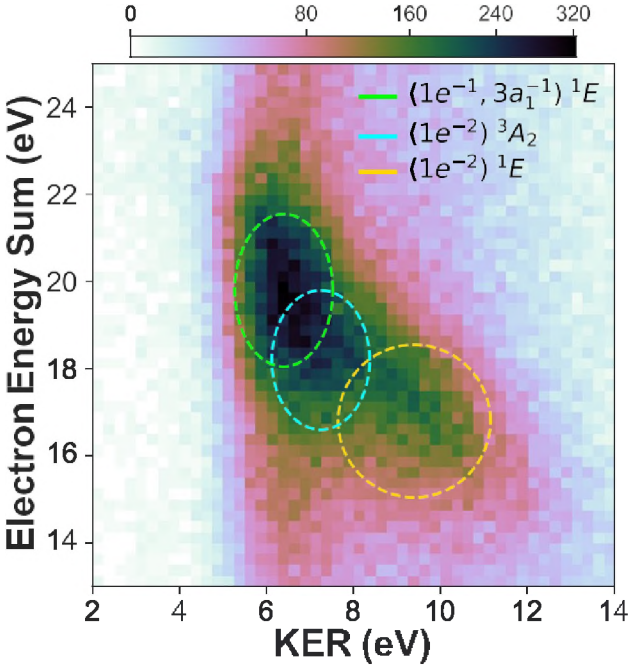

Figure 13. The $NH^+ + H^+ + H$ three-body yield, after PDI of NH_3 at 61.5 eV, as a function of the KER and the kinetic energy sum of the photoelectron pair. The three contributing dication states are color-coded (green, cyan, and gold) and shown as ellipses to guide the eye (they only approximately represent the software gates).

42 *Three-body breakup channel:* $NH^+ + H^+ + H$

As in the previous section, we plot in figure 12 the PDI yield of the $NH^+ + H^+ + H$ channel as a function of the kinetic

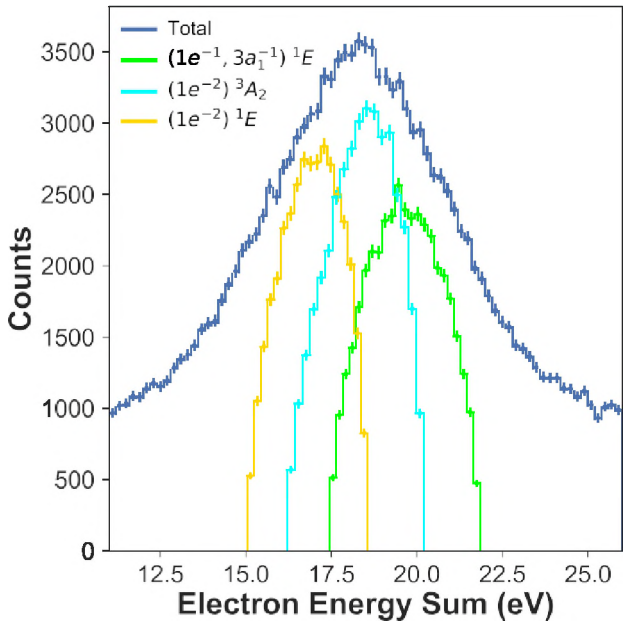

Figure 14. The $NH^+ + H^+ + H$ three-body yield, after PDI of NH_3 at 61.5 eV, as a function of the electron kinetic energy sum (shown in blue). The distributions for the three contributing dication states are shown in their respective color-codes (shown in green, cyan, and gold, and multiplied by a factor of 1.5 for improved visibility). Contributions from the individual dication states are extracted with gates as indicated in figure 13, and hence their sum does not reflect the total (blue) yield (see text).

energy of the first and second detected electrons, to produce the electron–electron energy correlation map. As before, the figure has been symmetrized across the diagonal (the line $E_1 = E_2$) to account for the indistinguishability of the two photoelectrons. With the guidance of the calculated PES cuts, we identify three features corresponding with three NH^{2+} dication electronic states that feed the three-body $NH^+ + H^+ + H$ fragmentation channel. Again, although these features are difficult to visually identify here, they are better separated in different spectra that are shown below in figure 13. The photoelectrons associated with these features have energy sums centered around 19.7 eV, 18.3 eV, and 16.8 eV, and a FWHM of roughly 2.5 eV, 2.3 eV, and 2.1 eV, respectively. These features, indicated by diagonal lines (taking the form $E_2 = E_1 + E_{sum}$), are color-coded as green, cyan, and gold to guide the eye (the same green color used in the two-body breakup section is applied here because the same dication state contributes to both the two- and three-body fragmentation channels, as discussed below). Using the same protocol as described in the two-body breakup section, we choose each of these three features by selecting carefully around the center of each feature in figure 13. As in the two-body breakup channel, these three states are accessed via direct PDI and also evidently through autoionization.

Three corresponding features are present in the electron–nuclei energy correlation map, shown in figure 13, which are circled by their respective color-codes to guide the eye (as before, these ellipses do not reflect the actual momentum gates). The feature circled by the cyan ellipse can be mistaken as a part of the feature circled by either the green or gold

ellipse, however, it is identified as a state with the assistance of the calculated PES cuts. Each feature possesses a different KER distribution centered around 6.4 eV, 7.1 eV, and 9.4 eV, each with a FWHM of roughly 1.1 eV, 1.4 eV, and 2.4 eV, respectively.

We present the $NH^+ + H^+ + H$ three-body yield as a function of the photoelectron energy sum in figure 14, where each feature we identified in figure 13 has been indicated by a distribution in its corresponding color. In the total yield we observe a slightly asymmetric monomodal distribution. As in the two-body channel, the wings on the distribution originate from false coincidences and background events that are challenging to completely eliminate in the analysis, causing a near-uniform background (clearly visible in figure 12) to underlie the spectrum, resulting in exaggerated wings.

Next, we show the $NH^+ + H^+ + H$ yield as a function of KER in figure 15, following the color code of figure 13. In the total yield we observe a broad asymmetric bimodal structure in the KER distribution. This bimodal distribution shows a rapid increase in yield on the low energy side of the peak and a slow decay in yield towards high KER, where the second mode is located. Both, the experimental and calculated photoelectron energy sums and KERs for each dication state are listed in table 3, showing good agreement for the $(1e^{-2})\ ^3A_2$ (cyan) and $(1e^{-2})\ ^1E$ (gold) dication states. In the case of the $(3a_1^{-1}, 1e^{-1})\ ^1E$ state (green), the agreement between experiment and theory is not as close, although the two values lie within the theoretically estimated FWHM. It is noteworthy that figure 1(b) indicates that the $(3a_1^{-1}, 1e^{-1})\ ^1E$ state possesses a barrier to dissociation when starting from the neutral equilibrium geometry, which is lifted when starting from geometries where the two N–H distances are compressed. This is consistent with the fact that for this state the calculated vertical photoelectron energy is greater than the measured value, whereas the calculated KER is smaller than the measured value. Consequently, PDI at geometries with contracted bond lengths are more likely to undergo three-body dissociation, as these excitations can directly fragment over the barrier. We point out that the difference in electron energy sum between the measurement and calculation is approximately the same as the difference in KER, which further supports this interpretation.

The three contributing dication states were also identified using MRCI calculations, as highlighted in the theory section, and are consistently color-coded throughout the paper, where the green state corresponds with the $(3a_1^{-1}, 1e^{-1})\ ^1E$ state (the same as in the two-body breakup section), the cyan state corresponds with the $(1e^{-2})\ ^3A_2$ state, and the gold state with the $(1e^{-2})\ ^1E$ state. The ion yield measurements estimate the branching ratios for these three dication states, listed in table 3, to be approximately 29%±4% for the $(3a_1^{-1}, 1e^{-1})\ ^1E$ state, 24%±4% for the $(1e^{-2})\ ^3A_2$ state, and 47%±4% for the $(1e^{-2})\ ^1E$ dication state. These branching ratios are derived in the same manner as described in the two-body breakup section. As before, the main contribution to the uncertainty of the branching ratio is rooted in the aforementioned electron pair dead-time, which influences the detection yield of the electron–ion coincidences for each dication state as a function

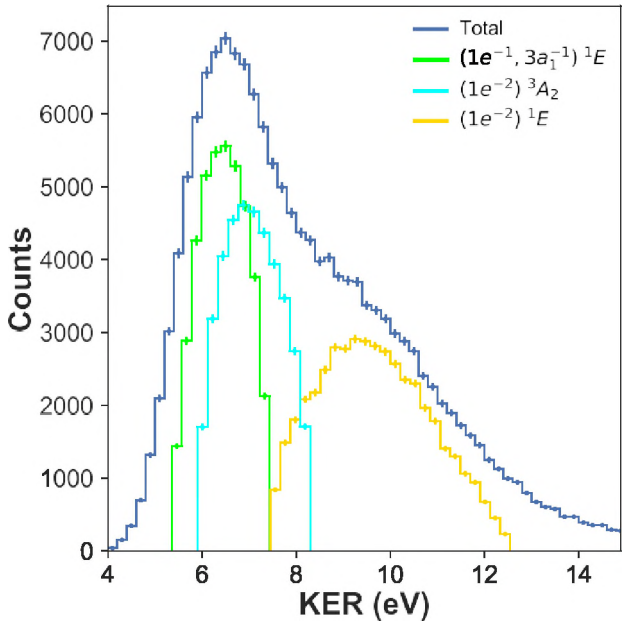

Figure 15. The $NH^+ + H^+ + H$ three-body yield, after PDI of NH_3 at 61.5 eV, as a function of the KER (shown in blue). The distributions for the three contributing dication states are shown in their respective color-codes (shown in green, cyan, and gold, and multiplied by a factor of 1.5 for improved visibility). Contributions from the individual dication states are extracted with gates as indicated in figure 13, and hence their sum does not reflect the total (blue) yield (see text).

of the electron sum energy. Applying the simulation mentioned above, we estimate the total possible loss in PDI yield for electron sum energies of 19.7 eV $[(3a_1^{-1}, 1e^{-1})\ ^1E]$, 18.3 eV $[(1e^{-2})\ ^3A_2]$, and 16.8 eV $[(1e^{-2})\ ^1E]$ to be 6.5%, 7.1%, and 7.9%, respectively. This translates to an error of up to 4% in the branching ratio. Errors due to deviations from the assumed Gaussian shape of each feature in the fitting process and the quality of the fit are estimated to be small (both $<1\%$).

The energetics observed in the PES cuts of figures 1(b) and 13, and table 3 indicate that the $(3a_1^{-1}, 1e^{-1})\ ^1E$ dication state dissociates to the $NH^+(^2\Pi) + H^+ + H(^2S)$ limit, with the $(1e^{-2})\ ^3A_2$ and $(1e^{-2})\ ^1E$ states dissociating to this very same limit. This finding suggests that following PDI of NH_3 to either of these E symmetry dication states, i.e., the $(3a_1^{-1}, 1e^{-1})\ ^1E$ and $(1e^{-2})\ ^1E$ states, three-body dissociation ensues on the A' symmetry PESs, shown in figure 1(b). In the case of the $(3a_1^{-1}, 1e^{-1})\ ^1E$ dication state, the A'' symmetry curve possesses a large barrier to dissociation, whereas fragmentation on the A' symmetry curve is much more favorable. As for the $(1e^{-2})\ ^1E$ state, we do not observe fragmentation on the A'' symmetry curve, although the PES cuts shown in figure 1(b) indicate that the excitation lies above the shallow barrier of this curve. However, similar to the case of the $(3a_1^{-1}, 1e^{-1})\ ^1E$ dication state the fragmentation on the A' symmetry curve is favored in the $(1e^{-2})\ ^1E$ state. Populating the $(1e^{-2})\ ^3A_2$ dication state results in direct three-body fragmentation on the PES (which is not doubly degenerate in the FC region like the E symmetry states), reaching the $NH^+(^2\Pi) + H^+ + H(^2S)$ limit. We point out that at large internuclear separations (>18 Bohr) a charge-exchange mechanism was observed between the

Table 3. The measured and calculated photoelectron energy sum and KER for each of the three active dication states leading to $NH^+ + H^+ + H$ fragmentation following PDI of NH_3 at 61.5 eV, as well as the estimated branching fractions and β_2 anisotropy parameter (see text).

State	Photoelectron Energy sum (eV)		KER (eV)		Branching fraction	β_2
	Experiment	Theory[a]	Experiment	Theory[a,b]		
$(3a_1^{-1}, 1e^{-1})\ ^1E$ (green)	19.7 (2.5)	21.0 (2.4)	6.4 (1.1)	5.2 (2.4)	29% ± 4%	−0.27 ± 0.01
$(1e^{-2})\ ^3A_2$ (cyan)	18.3 (2.3)	18.1 (3.3)	7.1 (1.4)	7.7 (3.3)	24% ± 4%	−0.17 ± 0.01
$(1e^{-2})\ ^1E$ (gold)	16.8 (2.1)	16.8 (3.4)	9.4 (2.4)	9.4 (3.4)	47% ± 4%	0.04 ± 0.01

[a] Theoretical FWHM values estimated from square of symmetric stretch vibrational wavefunction of NH_3 projected onto dication state (see text).
[b] Theoretical KER values are calculated assuming ro-vibrational ground state fragments, i.e., assuming maximum KER with no energy channeled into internal excitations.

NH^+ and H fragments in this dication state, which produces the fragments NH + H^+ + H^+ and is discussed in detail in [I]. An analogous asymptotic electron transfer mechanism has also been observed in dissociative electron attachment to NH_3 [39].

To determine if there are preferred molecular orientations where PDI of NH_3 occurs for each of the three dication states, we plot in figures 16(a)–(c) the yield of the $NH^+ + H^+ + H$ three-body fragmentation as a function of the cosine of the relative angle between the recoil axis of the charged fragments of the molecular breakup (NH^+–H^+) and the XUV polarization, ε. While in a three-body breakup all particles carry away momentum, we can deduce from the PIPICO spectrum, presented in figure 2, that for the most part the charged fragments solely compensate their momenta, while the third particle (the neutral H atom) takes on a spectator role. This becomes apparent by examining the TOF correlation of the $NH^+ + H^+ + H$ channel, which is almost as wide in the TOF difference and as narrow in the TOF sum as the $NH_2^+ + H^+$ two-body fragmentation. This underlines that the charged fragments of the three-body breakup repel each other and interact with each other via the Coulomb force over a long range of internuclear distances. Thus, their recoil axis, which is calculated via the difference of the measured momenta, appears to be an appropriate choice for a distinguished axis. We will see later that the relative angle between the charged fragments almost exclusively peaks at 180° and the neutral H fragment carries away rather little kinetic energy (figure 17), further supporting this selection.

Equation (1) is valid for any vectorial quantity arising from single-photon ionization of a randomly oriented sample by linearly polarized light. Consequently, it can be applied to the recoil axis of the charged fragments $H^+ + NH^+$ of the three-body breakup channel as well. For the $(3a_1^{-1}, 1e^{-1})\ ^1E$ and $(1e^{-2})\ ^3A_2$ dication states, we observe an enhancement in PDI for molecular orientations where the $NH^+ + H^+$ recoil axis is orientated at a 90° angle with respect to the polarization vector. As in the two-body breakup case, this roughly coincides with the C_{3v} symmetry axis of the molecule. We find a β_2 value of 0.27±0.01. In the $(3a_1^{-1}, 1e^{-1})\ ^1E$ dication state, the PDI involves the $3a_1$ orbital, which is aligned along the molecular C_{3v} axis. This could explain the enhancement in PDI at geometries where the polarization vector of the ionizing field is directed along this orbital, and why this enhancement is reduced in the $(1e^{-2})\ ^3A_2$, where the ionization no longer involves the $3a_1$ orbital. The β_2 value was determined to be 0.17±0.01. The anisotropy parameter for both states are also listed in table 3.

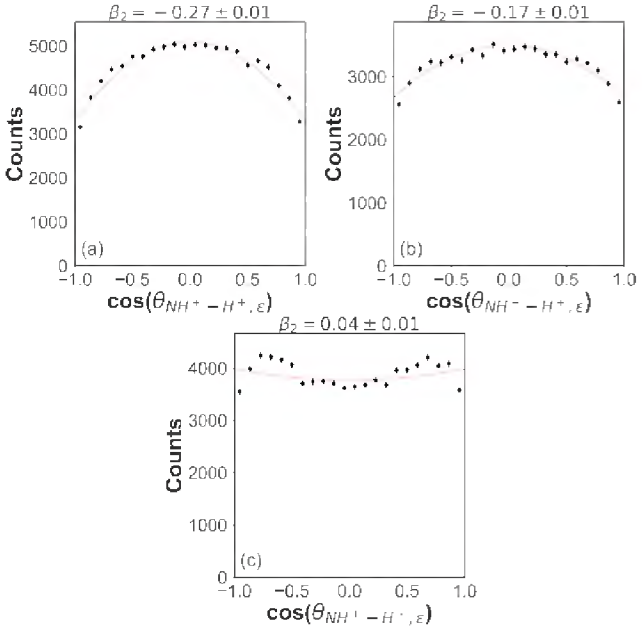

Figure 16. The $NH^+ + H^+ + H$ three-body fragmentation yield, after PDI of NH_3 at 61.5 eV, as a function of the cosine of the measured relative angle between the NH^+ –H^+ recoil axis and the XUV polarization vector, ε, for the (a) $(3a_1^{-1}, 1e^{-1})\ ^1E$, (b) the $(1e^{-2})\ ^3A_2$, and (c) the $(1e^{-2})\ ^1E$ dication states. The fits, representing the parametrizations in terms of the anisotropy [see equation (1)], are shown in red, where the retrieved β_2 value is shown above each plot.

In contrast, the $(1e^{-2})\ ^1E$ dication state appears to exhibit a small enhancement in PDI for orientations where the recoil axis of the charged NH^+ and H^+ fragments is orientated at a 35° and 145° angle with the polarization vector [see figure 16(c)]. The angular distribution is nearly isotropic, appearing almost flat, meaning that compared to the other two dication states of the three-body breakup, we observe a lower likelihood of PDI where the recoil axis of the charged fragments NH^+ and H^+ is orientated perpendicular to the polarization vector in the $(1e^{-2})\ ^1E$ state. Here, since the PDI of NH_3 no longer involves the $3a_1$ orbital, enhancement near the C_{3v} axis is suppressed. Because the PDI only involves the $1e$ orbital, which lies along the N–H bonds of the molecule, we observe an enhancement in PDI for molecular orientations near angles where the recoil axis of the charged fragments

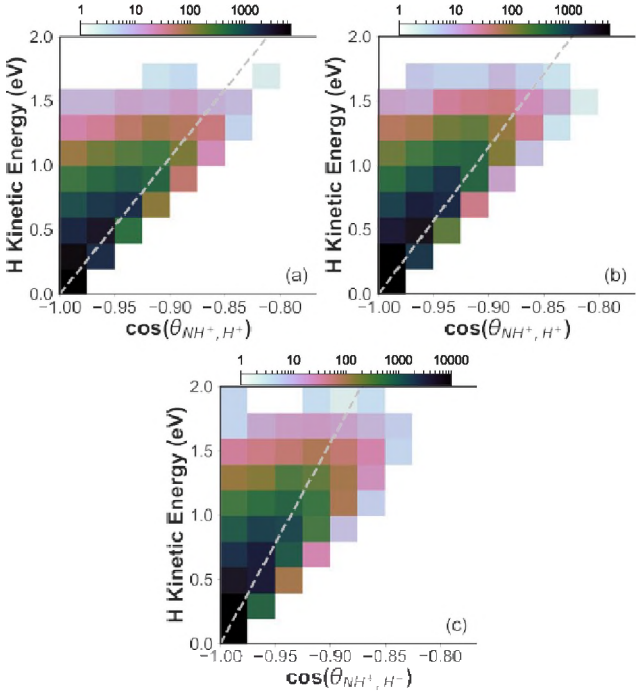

Figure 17. The $NH^+ + H^+ + H$ three-body fragmentation yield after PDI of NH_3 at 61.5 eV as a function of the cosine of the measured relative angle between the NH^+ and H^+ fragment momentum vectors and the kinetic energy of the neutral H fragment, for (a) the $(3a_1^{-1}, 1e^{-1})\ ^1E$, (b) the $(1e^{-2})\ ^3A_2$, and (c) the $(1e^{-2})\ ^1E$ dication states. The dashed silver line in each figure serves to guide to the eye towards the slope of the feature.

NH^+ and H^+ lies along the XUV polarization vector. We point out that this interpretation is qualitative and does not explain the aforementioned differences between the $(1e^{-2})\ ^3A_2$ and $(1e^{-2})\ ^1E$ states, which both invoke ionization from solely the 1*e* orbital. We find a β_2 value of 0.04±0.01.

The angular distribution of figure 16(c) may be influenced by a breakdown of the axial recoil approximation during the dissociation [40], which can occur for select dication states and has been identified in the PDI of water molecules for a similar photon energy recently [41]. Given the purely statistical error bars, the measured angular distribution for the $(1e^{-2})\ ^1E$ state is somewhat inconsistent with the β_2 functional form, while for the $(3a_1^{-1}, 1e^{-1})\ ^1E$ and $(1e^{-2})\ ^3A_2$ states, the angular distributions can be accurately fitted by equation (1). The inconsistency [figure 16(c)] is rather insensitive to fine details of the momentum calibration and does not appear to be subject to multi-hit problems of the ion and electron detectors, all of which were inspected thoroughly. We could not identify any problems in these analysis domains that could explain the small deviation of the measured angular distribution in figure 16(c) from the flat or shallow parabolic form of equation (1), but we need to point out that the KER and electron sum energy distributions for the weak $(1e^{-2})\ ^1E$ dication state are quite broad and may overlap with the distributions of the $(1e^{-2})\ ^3A_2$ dication state, as apparent in figure 13.

The diffuse features corresponding to the weak $(1e^{-2})\ ^1E$ dication state may also contain background contributions from false coincidences with parent NH_3^+ ions and background H^+ as well as H_2^+ ions (observed as the horizontal and vertical features in figure 2). Moreover, a small number of events from the $NH_2^+ + H^+$ two-body breakup channel, which lies adjacent to the $NH^+ + H^+ + H$ channel in the PIPICO spectrum (seen in figure 2), can be falsely assigned and may contribute to the two small peaks. The spread in TOF of the $NH_2^+ + H^+$ coincidence feature in figure 2 may result in a false assignment of some $NH_2^+ + H^+$ fragment pairs to any of the 3-body channels. Both of the latter two sources of background, although largely eliminated in the calibration and analysis, can be challenging to completely remove in some cases, which can result in select ionization channels being contaminated by a few per- cent of erroneously assigned events. Since the two small peaks in figure 16(c) lie only a few (~5%±1%) percent above the isotropic distribution, we speculate that these features arise from any of the three forms of pollution mentioned above, and do not point towards some unusual dissociation mechanism or previously unobserved photodissociation dynamics of the $(1e^{-2})\ ^1E$ dication state of NH_3.

In figure 17 we plot on a logarithmic scale the $NH^+ + H^+ + H$ three-body fragmentation yield, following the PDI of NH_3 by 61.5 eV photons, as a function of the cosine of the measured relative angle between the NH^+ and H^+ ion momenta, and the kinetic energy of the neutral H fragment. The triangular shape of the distribution is governed by momentum conservation of the three fragments, and we use it to elucidate the interaction between the heavy particles during the dissociation as a function of the NH_3^{2+} state. All three distributions are peaked at 180°, indicating a preferred back-to-back emission between the photoions with the neutral H largely spectating. However, as the H fragment receives more kinetic energy from the dissociation, the relative angle between the two NH^+ and H^+ ionic fragments correspondingly opens up, which becomes nicely apparent in this 2D-spectrum. We observe that the range of angles spanned between the two photoions, following the PDI to the $(3a_1^{-1}, 1e^{-1})\ ^1E$ and $(1e^{-2})\ ^3A_2$ dication states [figures 17(a) and (b)], is broader than in the $(1e^{-2})\ ^1E$ state [figure 17(c)]. The range of kinetic energies spanned by the neutral H fragment is broader in the $(1e^{-2})\ ^1E$ dication state [figure 17(c)] compared with the $(3a_1^{-1}, 1e^{-1})\ ^1E$ and $(1e^{-2})\ ^3A_2$ dication states [figures 17(a) and (b)]. We also observe a difference in the correlation between the kinetic energy of the neutral H and the measured relative angle between the NH^+ and H^+ photoions. The dashed silver lines in figures 17(a)–(c) are intended to guide the eye towards the slope of the features and improve the visibility of the energy-angle correlations. In the $(3a_1^{-1}, 1e^{-1})\ ^1E$ and $(1e^{-2})\ ^3A_2$ dication states [figures 17(a) and (b)] the angle between the NH^+ and H^+ fragments opens up more rapidly than in the $(1e^{-2})\ ^1E$ state [figure 17(c)], as the neutral H fragment takes away more kinetic energy. This suggests that the neutral H fragment acts more like a passive spectator in the dissociation that ensues following PDI to the $(1e^{-2})\ ^1E$ dication state as compared to the dissociation from the $(3a_1^{-1}, 1e^{-1})\ ^1E$ and $(1e^{-2})\ ^3A_2$ dication states, which show a stronger influence of the kinetic energy of the neutral H fragment on the relative angle between the photoions.

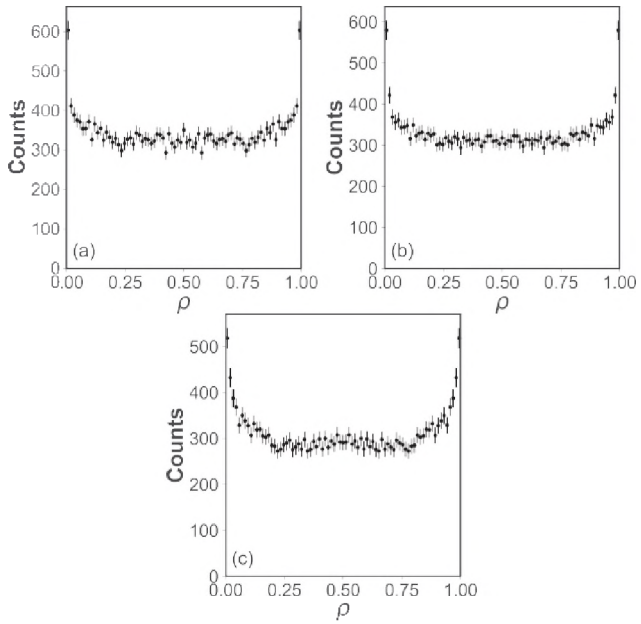

Figure 18. The $NH^+ + H^+ + H$ three-body fragmentation yield, after PDI of NH_3 at 61.5 eV, as a function of the electron energy sharing ρ (equation (2)) for the (a) $(3a_1^{-1}, 1e^{-1})\ ^1E$, (b) the $(1e^{-2})\ ^3A_2$, and (c) the $(1e^{-2})\ ^1E$ dication states.

Next, we display the $NH^+ + H^+ + H$ three-body fragmentation yield as a function of the energy sharing between the two photoelectrons for the three features that correspond with the three dication states. These results are shown in figures 18(a)–(c). As before, we attribute the sharp features near 0 and 1, observed in figures 18(a)–(c), to an autoionization process, corresponding with a fast photoelectron and slow electron emerging from autoionization. The fraction of PDI via autoionization relative to direct PDI is ~5.6%±2.0% in the $(3a_1^{-1}, 1e^{-1})\ ^1E$ state, ~7.6%±1.1% in the $(1e^{-2})\ ^3A_2$ state, and ~7.7%±2.1% in the $(1e^{-2})\ ^1E$ dication state. This fraction is estimated using the same protocol described in the two-body breakup section.

Lastly, we plot in figures 19–21 the $NH^+ + H^+ + H$ three-body fragmentation yield as a function of the cosine of the relative emission angle between the two photoelectrons, (a) integrated over all energy sharing conditions and (b) in an equal energy sharing condition for the three dication states. There are no conditions enforced on either the molecular orientation nor the emission angle of the first detected photo- electron relative to the polarization vector of the XUV beam. In the equal energy sharing case the relative angle is plot- ted for $0.425 < \rho < 0.575$. As pointed out in the two-body breakup section, our measurement suffers from some multi- hit detector dead-time effects, influencing the measured yield of photoelectrons emitted in the same direction with similar kinetic energies. In the equal energy sharing condition and for $\theta_{e_1,e_2} \leq 90°$ this corresponds with a maximum loss of 20% of the events for the $(3a_1^{-1}, 1e^{-1})\ ^1E$ state, 21% for the $(1e^{-2})\ ^3A_2$ state, and 23% for the $(1e^{-2})\ ^1E$ state. Like in the two-body breakup case we believe that the actual loss is at least a factor of two smaller than the

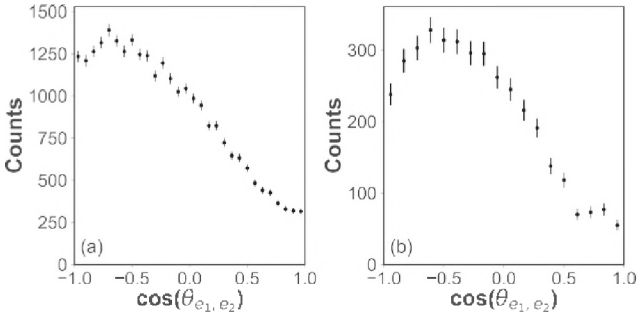

Figure 19. The $NH^+ + H^+ + H$ three-body fragmentation yield, after PDI of NH_3 at 61.5 eV, as a function of cosine of the relative emission angle between the two photoelectrons for the $(3a_1^{-1}, 1e^{-1})\ ^1E$ dication state, (a) integrated over all possible electron energy sharing and (b) for equal energy sharing ($\rho = 0.5 \pm 0.075$).

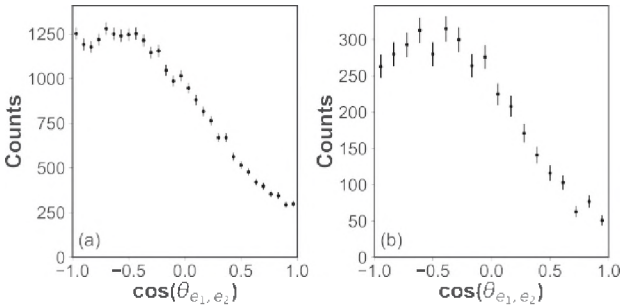

Figure 20. The $NH^+ + H^+ + H$ three-body fragmentation yield, after PDI of NH_3 at 61.5 eV, as a function of the cosine of the relative emission angle between the two photoelectrons in two different energy sharing conditions for the $(1e^{-2})\ ^3A_2$ dication state, (a) integrated over all possible electron energy sharing and (b) for equal energy sharing ($\rho = 0.5 \pm 0.075$).

worst-case scenario listed above, i.e., closer to our simulated results for the unequal electron energy sharing case. As in the two-body breakup section, we refrain from showing the photoelectron angular distribution of the unequal energy sharing case, which captures the autoionization feature, as there is a significant contribution due to direct PDI that significantly pollutes the autoionization signal and prevents a clear analysis of this relative angular distribution.

The relative angles between the two electrons, integrated over all energy sharing cases, show a preferred emission of the two particles into opposite hemispheres. The distribution for the $(3a_1^{-1}, 1e^{-1})\ ^1E$ dication state [figure 19(a)] peaks at 135° with a notable dip at 180° corresponding to a back-to-back emission. The $(1e^{-2})\ ^3A_2$ state [figure 20(a)] peaks at 130° with a slight increase at 180° compared to the $(3a_1^{-1}, 1e^{-1})\ ^1E$ dication state. The $(1e^{-2})\ ^1E$ state [figure 21(a)] has a peak at 120°, but now exhibits dominating back-to-back emission between the two electrons.

The photoelectron dynamics in the equal energy sharing condition [figures 19(b)–21(b)], again, reveals similar anisotropic angular distributions, which possess node-like features near 0° relative electron–electron emission angle and a peak at approximately 125° for the $(3a_1^{-1}, 1e^{-1})\ ^1E$ state, 115° for the $(1e^{-2})\ ^3A_2$ state, and 120° for the $(1e^{-2})\ ^1E$ state. A

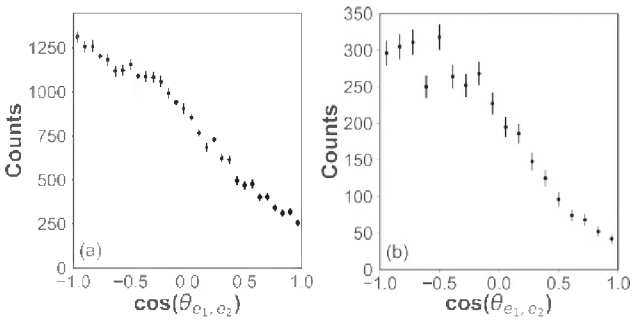

Figure 21. The $NH^+ + H^+ + H$ three-body fragmentation yield, after PDI of NH_3 at 61.5 eV, as a function of the cosine of the relative emission angle between the two photoelectrons in two different energy sharing conditions for the $(1e^{-2})$ ^1E dication state, (a) integrated over all possible electron energy sharing and (b) for equal energy sharing ($\rho = 0.5 \pm 0.075$).

dip at 180° remains visible. All three dication states resemble the dynamics of a knock-out double ionization process. In all three cases, the likelihood for an emission of the two electrons in the same direction is roughly a factor of 10 less likely than the emission at peak angle.

5. Conclusion

In this experiment we performed state-selective measurements on the two-body $NH_2^+ + H^+$ and three-body $NH^+ + H^+ + H$ dissociation channels of neutral NH_3, following PDI at 61.5 eV, where the two photoelectrons and two cations were detected in coincidence on an event-by-event basis using charged particle 3D momentum imaging. With the help of theory, five dication states could be identified as active in this photon energy range and assigned to the two different breakup channels. Three of these PDI channels produce ro-vibrationally excited ionic fragments, where the $(3a_1^{-1}, 1e^{-1})$ ^1E and $(3a_1^{-1}, 1e^{-1})$ ^3E dication states lead to hot NH_2^+ fragments, while the $(1e^{-2})$ $^3A_2$ dication state leads to a hot NH^+ fragment.

Our measurement identifies three dication electronic states that dissociate to $NH_2^+ + H^+$ fragments, which are populated via direct PDI as well as through autoionization. We observe that the initial excitations in one of these dication states, the $(3a_1^{-2})$ $^1A_1$ state, undergoes intersystem crossing preceding dissociation. This effect has been observed before, but only close to the PDI threshold. By plotting the relative angle between the recoil axis of the molecular breakup and polarization vector of the XUV beam, we see an anisotropic PDI yield that illustrates the connection between the molecular orbitals participating in the PDI and the molecular orientations experiencing enhanced PDI.

In the three-body dissociation channel of NH_3^{2+} we identify three contributing dication states, two of which are different from the states of the two-body breakup channel, that dissociate to $NH^+ + H^+ + H$ fragments. However, these states are also populated via the same ionization mechanisms, i.e., direct PDI and autoionization. In contrast to the two-body fragmentation channel, in this three-body breakup channel we observe that the three contributing dication states directly dissociate without any non-adiabatic transitions preceding the fragmentation. Plotting the relative angle between the recoil axis of the charged fragments of the breakup and the polarization vector of the XUV beam again demonstrates the connection between the molecular orbitals participating in the PDI and the molecular orientations experiencing enhanced PDI. Moreover, the dissociation of the two dication states of the three-body fragmentation result in different spectator roles of the neutral H atom.

Lastly, we presented the relative electron–electron angular distribution of all dication electronic states for all and equal electron–electron energy sharing. The distributions indicate the dominance of a knock-out PDI mechanism in all cases, and they are similar to the kinematics reported for the PDI of atoms (He) and small molecules (D_2 and H_2O) for comparable excess energies [35, 36, 42, 43].

Acknowledgments

Work at LBNL was supported by the U.S. Department of Energy, Office of Science, Office of Basic Energy Sciences, Division of Chemical Sciences, Biosciences, and Geosciences under contract No. DE-AC02-05CH11231 and used the Advanced Light Source and National Energy Research Computing Center. JRML personnel were supported by the same US DOE funding source under Award No. DE-FG02-86ER13491. AG was supported by the ALS through a Doc- toral Fellowship in Residence. Personnel from the University of Nevada, Reno was supported by the National Science Foundation Grant No. NSF-PHY-1807017. The Frankfurt group acknowledges the support of the Deutsche Akademische Austausch Dienst (DAAD) and the Deutsche Forschungsgemein-schaft (DFG). We thank the staff at the Advanced Light Source for operating beamline 10.0.1.3 and providing the photon beam. Moreover, we thank the RoentDek GmBH for longtime support with detector hardware and software.

References

[1] Gaire B *et al* 2015 Auger decay and subsequent fragmentation pathways of ethylene following *k*-shell ionization *Phys. Rev.* A **92** 013408
[2] Gaire B *et al* 2014 Hydrogen and fluorine migration in photo-double-ionization of 1, 1-difluoroethylene (1, 1-$C_2H_2F_2$) near and above threshold *Phys. Rev.* A **89** 043423
[3] Gaire B *et al* 2014 Photo-double-ionization of ethylene and acetylene near threshold *Phys. Rev.* A **89** 013403
[4] Yarkony D R 1996 Diabolical conical intersections *Rev. Mod. Phys.* **68** 985

[5] Winkoun D and Dujardin G 1986 Fragmentation of doubly charged ammonia cations NH_3^{2+} studied by the photoion-photoion coincidence (PIPICO) method *Z. Phys.* D **4** 57–64

[6] Stankiewicz M, Hatherly P A, Frasinski L J, Codling K and Holland D M P 1989 The double photoionisation of NH_3 using the triple coincidence (PEPIPICO) technique *J. Phys. B: At. Mol. Opt. Phys.* **22** 21–31

[7] Locht R, Davister M, Denzer W, Jochims H W and Baumgärtel H 1989 About the double ionization of ammonia and carbon dioxide. A comparison between photoionization and electron impact *Chem. Phys.* **138** 433–40

[8] Locht R and Momigny J 1987 The double ionization of ammonia. Its dissociation into the doubly ionized fragment N_2^+ *Chem. Phys. Lett.* **138** 391–6□

[9] Eland J H D 2006 Double photoionisation spectra of methane, ammonia and water *Chem. Phys.* **323** 391–6

[10] Tarantelli F, Tarantelli A, Sgamellotti A, Schirmer J and Cederbaum L S 1985 On the doubly ionized states of ammonia *Chem. Phys. Lett.* **117** 577–82

[11] Samson J A R, Haddad G N and Kilcoyne L D 1987 Absorption and dissociative photoionization cross sections of NH_3 from 80 to 1120 Å *J. Chem. Phys.* **87** 6416–22

[12] Appell J and Horsley J A 1974 Electronic states of doubly ionized ammonia *J. Chem. Phys.* **60** 3445–8

[13] Märk T D, Egger F and Cheret M 1977 Ionization of ammonia and deuterated ammonia by electron impact from threshold up to 180 eV *J. Chem. Phys.* **67** 3795–802

[14] Langford M L, Harris F M, Fournier P G and Fournier J 1992 Determination of singlet- and triplet-state energies of the doubly ionized ammonia molecule by double-charge-transfer spectroscopy *Int. J. Mass Spectrom. Ion Process.* **116** 53–69

[15] Griffiths W J and Harris F M 1990 An experimental determination of the energy of the first triplet doubly-ionized state of ammonia *Rapid Commun. Mass Spectrom.* **4** 366–8

[16] Locht R, Servais C, Ligot M, Derwa F and Momigny J 1988 The dissociative electroionization of ammonia and ammonia-D_3. I. The NH^+ and NH_2^+ dissociation channels *Chem. Phys.* **123** 443–54

[17] White J M, Rye R R and Houston J E 1977 Experimental auger electron spectrum of ammonia *Chem. Phys. Lett.* **46** 146–50

[18] Camilloni R, Stefani G and Giardini-Guidoni A 1977 The measured Auger electron spectrum of ammonia vapor *Chem. Phys. Lett.* **50** 213–7

[19] Økland M T, Fægri K Jr and Manne R 1976 Calculated Auger emission spectrum of ammonia *Chem. Phys. Lett.* **40** 185–8

[20] Dwight R J 1981 Initial-state relaxation effects in molecular Auger spectra *Phys. Rev.* A **23** 1215

[21] Boyd R K, Singh S and Beynon J H 1985 Delayed predissociation and collision-induced processes of the ammonia dication NH_3^{2+} *Chem. Phys.* **100** 297–314

[22] Ishihara T, Hino K and McGuire J H 1991 Photoionization of two electrons in helium *Phys. Rev.* A **44** R6980

[23] Larsen K A *et al* 2020 Photoelectron and fragmentation dynamics of the $H^+ + H^+$ dissociative channel in NH_3 following direct single-photon double ionization *Phys. Rev. Res.* **2** 043056

[24] Dörner R, Mergel V, Jagutzki O, Spielberger L, Ullrich J, Moshammer R and Schmidt-Böcking H 2000 Cold tar- get recoil ion momentum spectroscopy: a 'momentum microscope' to view atomic collision dynamics *Phys. Rep.* **330** 95–192

[25] Ullrich J, Moshammer R, Dorn A, Dörner R, Schmidt L P H and Schmidt-Böcking H 2003 Recoil-ion and electron momentum spectroscopy: reaction-microscopes *Rep. Prog. Phys.* **66** 1463

[26] Jagutzki O *et al* 2002 Multiple hit readout of a microchannel plate detector with a three-layer delay-line anode *IEEE Trans. Nucl. Sci.* **49** 2477–83

[27] Czasch A, Jahnke T and Shoeffler M 2008 *LMF2Root v1.6* https://atom.uni-frankfurt.de/czasch/default_files/software/LMF_tools/lmf2root/

[28] Jahnke T 2013 *LMF2Root 2 in a Nutshell LMF2Root Documentation*

[29] Rescigno T N and Schneider B I 1988 *J. Phys. B: At. Mol. Opt. Phys.* **21** L691

[30] Vanroose W, Horner D A, Martín F, Rescigno T N and McCurdy C W 2006 Double photoionization of aligned molecular hydrogen *Phys. Rev.* A **74** 052702

[31] Zare R N 1988 *Angular Momentum* (*Understanding Spatial Aspects in Chemistry and Physics*) Vol 33 (New York: Wiley)

[32] Greene C H and Zare R N 1982 Photofragment alignment and orientation *Annu. Rev. Phys. Chem.* **33** 119–50

[33] Liu X-J, Lucchese R R, Grum-Grzhimailo A N, Morishita Y, Saito N, Prümper G and Ueda K 2007 Molecular-frame photoelectron and electron-frame photoion angular distributions and their interrelation *J. Phys. B: At. Mol. Opt. Phys.* **40** 485–96

[34] Bradley E 1992 Bootstrap methods: another look at the Jackknife *Breakthroughs in Statistics* (Berlin: Springer) pp 569–93

[35] Bräuning H *et al* 1998 Absolute triple differential cross sections for photo-double ionization of helium—experiment and theory *J. Phys. B: At. Mol. Opt. Phys.* **31** 5149–60

[36] Weber T *et al* 2004 Fully differential cross sections for photo-double-ionization of D_2 *Phys. Rev. Lett.* **92** 163001

[37] Weber T *et al* 2004 Complete photo-fragmentation of the deuterium molecule *Nature* **431** 437–40

[38] Akoury D *et al* 2007 The simplest double slit: interference and entanglement in double photoionization of H_2 *Science* **318** 949–52

[39] Rescigno T N, Trevisan C S, Orel A E, Slaughter D S, Adaniya H, Belkacem A, Weyland M, Alexander D and McCurdy C W 2016 Dynamics of dissociative electron attachment to ammonia *Phys. Rev.* A **93** 052704

[40] Rakitzis T P and Zare R N 1999 Photofragment angular momentum distributions in the molecular frame: determination and interpretation *J. Chem. Phys.* **110** 3341–50

[41] Streeter Z L, Yip F L, Lucchese R R, Gervais B, Rescigno T N and McCurdy C W 2018 Dissociation dynamics of the water dication following one-photon double ionization. I. Theory *Phys. Rev.* A **98** 053429

[42] Randazzo J M, Turri G, Bolognesi P, Mathis J, Ancarani L U and Avaldi L 2020 Photo-double-ionization of water at 20 eV above threshold *Phys. Rev.* A **101** 033407

[43] Knapp A *et al* 2005 Photo double ionization of helium 100 eV and 450 eV above threshold: III. Gerade and ungerade amplitudes and their relative phases *J. Phys. B: At. Mol. Opt. Phys.* **38** 645–57